CIMAC CONGRESS 25
ZURICH, MAY 19 – 23, 2025

2025 | 258

Design, modeling and performance of an OMT methanol port fuel injector for large marine engines

Fuel Injection & Gas Admission and Engine Components

Marco Ferro, OMT - Officine Meccaniche Torino SpA

Simone Galuppini, OMT - Officine Meccaniche Torino SpA
Marco Coppo, OMT - Officine Meccaniche Torino SpA
Qiyan Zhou, Accelleron Switzerland Ltd
Gilles Hardy, Accelleron Switzerland Ltd

ABSTRACT

In order to accelerate the decarbonization of the marine transport sector to meet the most recent IMO targets, it is necessary to address the retrofit of as many existing engines as possible. In this respect, port fuel injection, i.e., the introduction at low pressure (10 – 50 bar) of fuel in the intake manifold to create a homogeneous mixture that burns according to the Otto cycle, allows the conversion to methanol operation with simpler and cheaper modifications to the engine.

In this context, the paper presents the design of a port fuel injector developed by OMT for large medium-speed engines. It features a solenoid actuated, outward opening conical poppet design producing a conical sheet of fluid that breaks up within a short distance from the nozzle due to the thinning of the liquid layer. To maximise atomization, care was taken into minimising internal pressure losses, while safety operation was ensured through a full double wall design with integrated flow limiter valve.

The resulting spray was characterized in a quiescent chamber using high-speed imaging to visualise its shape and determine angle and penetration, and Phase Doppler Anemometry techniques to measure the resulting droplet size through the estimation of the Sauter Mean Diameter. This was done using both methanol and water to establish a correlation useful to avoid the need to always use a toxic liquid like methanol for performing subsequent analyses of sprays obtained with nozzles of different shapes.

A detailed CFD model was then developed in cooperation with Accelleron to correctly simulate the characteristics of the spray produced by the injector. A good correlation between model and experiments was achieved, enabling the use of simulation tools for estimating the interaction between spray and intake air flow, which is crucial to achieve optimal fuel-air mixture, and thus accelerating the development of nozzle variants suitable to satisfy the individual needs of each customer.

Dedicated performance and endurance test rigs were designed and built to fully characterize the operation of the injector. In particular, an endurance test rig was developed in cooperation with Alfa Laval for the purpose of testing the components in conditions mimicking engine operation. Rig layout and main technical features are also presented and discussed, together with the experience gained from these tests.

Finally, the paper reports the results of the engine tests performed using the OMT port fuel injector.

1 INTRODUCTION

In July 2023, the International Maritime Organization (IMO) significantly raised the standards for the marine industry by updating its strategy to reduce greenhouse gas (GHG) emissions from ships [1]. This revision introduced more ambitious targets, aiming for net-zero emissions by 2050. Given that ships typically have a lifespan of 30 years, this means that the global fleet which will need to meet this target will largely consist of vessels built within the next decade. This realization has prompted ship owners to carefully consider their future investments, increasing the pressure on vessel and engine designers to quickly develop commercially viable solutions that can operate on synthetic renewable fuels like methanol and ammonia [2].

Additionally, the IMO's strategic document set GHG reduction targets for 2030 (a 30% reduction compared to 2008) and 2040 (an 80% reduction). Retrofitting will be the predominant means of achieving the 2030 target, at least, considering the existing global fleet is, on average, about midway through its lifespan, and needs upgrading to meet new efficiency and emissions regulations. Also, new build, dual fuel ships running on carbon-neutral fuels are just beginning to emerge and will take several years to have a sizable impact on decarbonization. Therefore, the industry must support decarbonization by providing cost-effective retrofit kits to rapidly scale up conversion projects.

According to DNV [3], methanol from renewable sources will be available sooner than ammonia. Moreover, methanol is less toxic than ammonia and easier to handle, as it can be stored in liquid form at ambient pressure, making it the preferred fuel for first-wave conversion projects.

For methanol, both port fuel injection (PFI) with lean-burn premixed combustion and high-pressure direct injection with diffusive combustion are technically feasible.

In lean-burn premixed combustion, liquid fuel is introduced into the intake manifold through port fuel injectors operating at low pressure (10-30 bar). Due to the large latent heat of methanol, just a small portion evaporates in the intake port (~20%), while most of it evaporates during the intake and compression stroke (~80%). [4] For this reason, the injectors need to produce a fine atomization of the liquid jet, so that the droplets can uniformly mix with and be easily transported by the air flow, and enter the combustion chamber, without wetting the intake duct walls. The air/fuel mixture is then ignited by a pilot injection of diesel fuel from the standard injector. In the dual fuel engine, the standard diesel injector is also used for full diesel operation, when methanol is unavailable.

In contrast, direct injection of methanol into the combustion chamber requires dedicated high-pressure injectors (typically 600-800 bar) and an expensive pumping system to pressurize the fuel. As the space on the cylinder head is already limited, the integration of diesel and methanol injectors into one object is very challenging and leads to custom-made and thus more expensive solutions.

Direct injection technology offers higher engine efficiency and a better fuel substitution ratio, because it requires smaller pilot injections for stable methanol combustion compared to port fuel injection, as reported in detail in [5] and [6]. Additionally, the diffusive combustion approach of high-pressure direct injection limits the contact of unburnt fuel with cylinder liner walls, reducing issues related to engine oil contamination as well as piston/liner scuffing due to oil film breakup.

However, because port fuel injection systems have simpler components and are easier to install, they offer a more practical method of retrofitting older vessels to operate on methanol, and represent a breakthrough in accelerating the industry's energy transition.

OMT has therefore developed an innovative PFI system which represents a significant advancement in retrofit technology. Operating at relatively low pressure (10-50 bar), the system creates a homogeneous fuel-air mixture that enables efficient Otto cycle combustion. The new PFI design guarantees optimal spray atomization, as shown through Phase Doppler Anemometry in quiescent air, and advanced CFD calculation in engine-like conditions.

This development is particularly significant, given the massive scale of the existing fleet. With over 100,000 commercial vessels in operation, [7] retrofit solutions that enable older vessels to benefit from carbon-neutral fuel use could be pivotal to accelerating the maritime energy transition and achieving net zero.

The paper presents the challenges faced during design and how they were addressed, as well as reporting injector performance data, both in terms of dynamics and of spray quality. Since experimental data on the spray quality could be obtained exclusively in quiescent air, we also present the results of a CFD model of the spray, developed in cooperation with our parent company Accelleron. The CFD model provides a simulation of spray behavior in engine-like conditions, both in

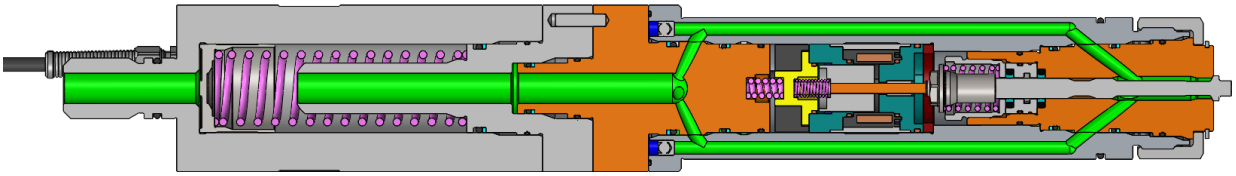

Figure 1: OMT PFI injector

terms of droplet size distribution and spray penetration, and including different orientations of the injector with respect to the charge air flow, considering different fuel and intake air temperatures.

2 OMT METHANOL PORT FUEL INJECTOR

2.1 Injector architecture

The injector is designed for a multi-point injection layout, i.e. with one injector for each cylinder, with a methanol supply pressure of 30 bar and for an engine power up to 1200 kW/cylinder. A section view of the injector and of its main components is shown in Figure 1. The paper presents the challenges faced during design and how they were addressed, as well as reporting injector performance data, both in terms of dynamics and of spray quality. Since experimental data on the spray quality could be obtained exclusively in quiescent air, we also present the results of a CFD model of the spray, developed in cooperation with our parent company Accelleron. The CFD model provides a simulation of spray behavior in engine-like conditions, both in terms of droplet size distribution and spray penetration, and including different orientations of the injector with respect to the charge air flow, considering different fuel and intake air temperatures. To limit the complexity of the engine interface, the injector is directly actuated by a solenoid, so that fuel return or control oil feeding and return lines are not needed. All potential leakages are directed towards a dedicated line with a low positive pressure of nitrogen or in vacuum, to avoid the possibility of formation of an explosive mixture, making the injector ATEX compliant. Finally, an inbuilt flow fuse limits the injected quantity in case of malfunctioning.

To maximize the atomization of the fuel with the limited differential pressure available, an outward-opening poppet valve architecture was chosen. Although the injection duration is approximately three times larger than for the case of direct injection, due to the much lower supply pressure a much larger fuel passage section is required. However, since with given fluid characteristics, injection pressure and downstream conditions, the size of the droplets is proportional to the characteristic dimension of the liquid jet forming at the nozzle outlet (see e.g. [8] and [9]), for this particular application, an implementation similar to that of high-pressure injectors, i.e. with holes open in a sac downstream of the needle seat, would require a very high number of holes to obtain a thickness of the liquid film comparable to the one that can be created at the exit of a poppet valve. As shown in Figure 2, thanks to a particularly narrow and long exit section of the poppet, it is possible to generate a liquid film with a thickness of less than 0.6 mm, which, in turn, is able to generate a spray with very fine droplets.

Moreover, for this layout almost all the pressure available is used to generate fluid velocity, while in a traditional architecture some pressure is lost at the needle seat, especially considering that the maximum stroke of the needle is limited by the

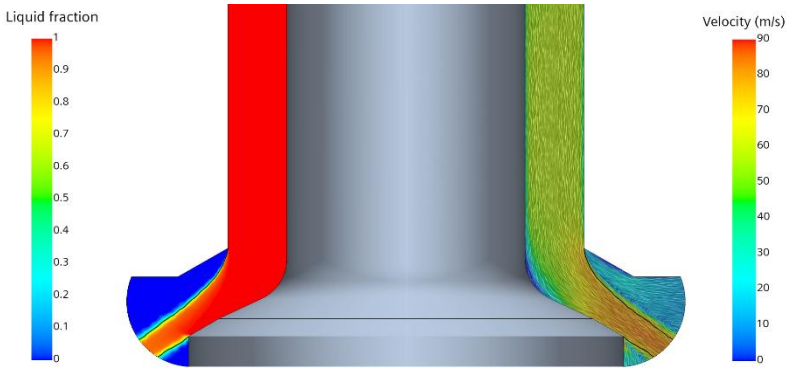

Figure 2: CFD simulation results of fuel flux at the injector exit in still air. Velocity field (*right*) and liquid fraction (*left*).

magnetic force available at the solenoid. Another advantage of the outward opening architecture is that it is possible to balance the fuel pressure forces on the needle, so that the actuator needs to counteract spring and inertia forces only, limiting the size and cost of the solenoid and, consequently, those of the injector. Additionally, in this configuration the intake manifold pressure acts in the direction of closing the needle, increasing the force on the seat and providing additional robustness against injector leakage.

A possible drawback of this architecture is that it is not possible to orient the spray with respect to the injector axis. However, the spray cone angle was chosen to be large (120°) to minimize the risk of fuel impacting the manifold walls and, as shown in the installation study reported in §3.4.2, the fuel impingement can be considerably reduced with a small inclination of the injector axis.

2.2 Injector Performance

A dedicated test bench (see Figure 3) was designed and procured to test and validate the PFI injectors. It allows the injection of test oil or distilled water into a chamber filled with air at a configurable pressure, thereby simulating the actual injection conditions of an engine intake manifold. The water temperature can be regulated up to 70°C to achieve conditions analogous to methanol in terms of dynamic viscosity and vapor pressure. This ensures accurate testing of the injector's performance under similar lubrication and cavitation conditions as in methanol operation. Optical access to the spray chamber is allowed through a glass panel, so that investigation on the spray formation and evolution can be conducted in-house. The measurement is fully automated and allows the acquisition of the mean injected mass and of the instantaneous needle lift, from which the injection rate shape of each shot can be reconstructed, allowing for the determination of the shot-to-shot dispersion of the injector.

Figure 3: PFI injector test bench (*left*), detailed view of the injection chamber (*right*).

Figure 4 shows a comparison between experimental results and data obtained from a 1D-simulation of the injector, performed with *GT-Suite*. Given the quite low operating pressure range, the behavior of the injector is significantly affected by the geometrical characteristics of the upstream feeding line, which, for this reason, were included in the model. A very good agreement between simulated and tested injector lift can be observed. Moreover, it can be noted that a small part-to-part variation of injection performance was obtained; in fact, the dispersion for a rated injection is limited to ±2% of injected mass. Excellent shot-to-shot variation was also achieved, with a 3σ variation of the injected mass smaller than 0,9% for a rated injection.

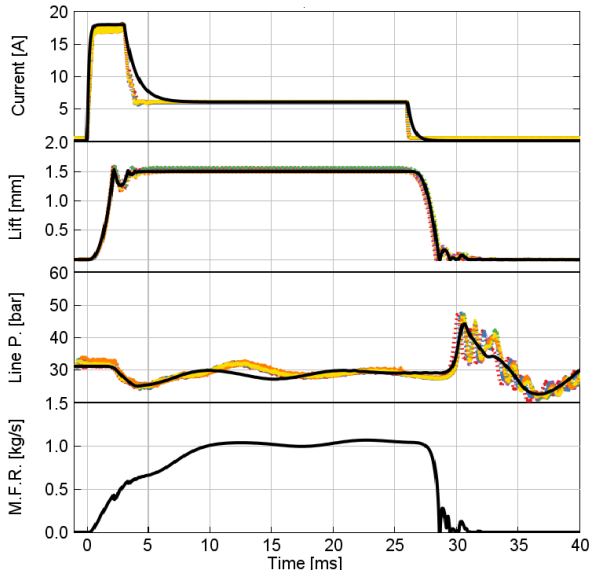

Figure 4: Comparison of simulation data (*black solid line*) with experimental results of 6 different injectors (*dotted colored lines*) for a rated injection.

Once the 1D-model is validated with test bench results, it is possible to perform a simulation of the injector performance on the engine, to account for the actual geometry of the feeding line. Figure 5 shows a comparison between simulated injector operation on the test bench and in the engine layout. It can be noticed how the difference in the pressure fluctuations in the upstream line considerably affects the injection rate shape and the total injected mass, highlighting the need for a differentiation of these two operation conditions when validating experimental data.

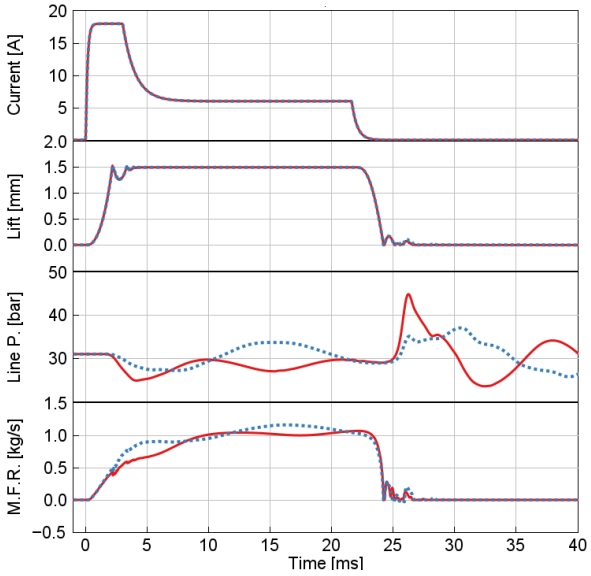

Figure 5: Simulation results considering the upstream feeding line of the test bench (*solid line*) vs. the actual engine layout (*blue dotted line*).

2.3 Injector Validation

2.3.1 Endurance test bench

To complete the validation of PFI injectors, a test bench was designed by Alfa Laval for durability testing (see Figure 6).

Figure 6: PFI injectors endurance test bench.

This bench can install up to five injectors which can operate under the same test conditions as the engine in terms of injection frequency and injection duration. Considering that the installed water pump has a maximum flow rate of 50 l/min, an accelerated test is also possible. The distilled water temperature can be adjusted up to 70°C, while the supply pressure can be adjusted between 10 bar and 50 bar. The injection of distilled water occurs in a tank filled with compressed air at settable pressure values between 1 bar and 6 bar. The average injection flow rate is continuously monitored by a Coriolis flow meter installed upstream of the injectors. The bench can be controlled remotely and is equipped with a fault diagnosis system, allowing it to operate 24/7 without the need for human supervision.

2.3.2 Engine tests

The injectors have cumulated 350 hours in methanol operation on a full scale laboratory engine, allowing for a substitution rate greater than 97% at 85% engine load. No performance or functional problem was reported by the engine maker and no significant wear or performance deviation was observed during an inspection performed on several injectors after 90 running hours on engine (see e.g. Figure 7).

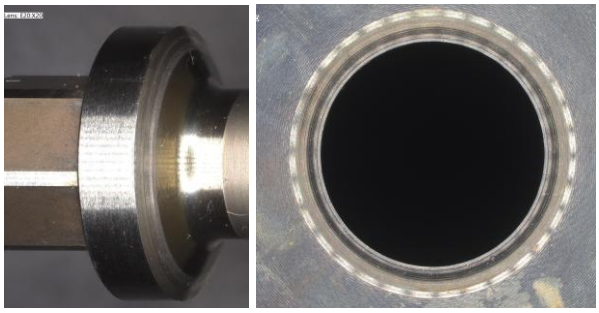

Figure 7: Needle (*left*) and needle seat (*right*) after 90 hours of engine tests.

3 SPRAY ANALYSIS

3.1 Experimental setup and measurement procedures

To characterize the spray generated by the injector, it was tested in a newly developed test bench at FVTR in Rostock, designed for droplet sizing and spray visualization of methanol sprays. The sprays can be measured in quiescent air at ambient pressure and temperature. The test cell shown in Figure 8 consists of a stainless-steel tank, fitted with multiple windows for the Phase Doppler Interferometry (PDI) system and for the high-speed camera. While the measurement system is fixed in space, the injector is positioned by a 2-axis traverse, allowing measurements from 90 to 370 mm nozzle distance.

Methanol or water are pressurized by an air-driven piston pump, and the fluid is stored in a pneumatic accumulator close to the injector with a volume of 0,46 liters. The test chamber pressure is kept very slightly below the atmospheric level as a part of the safety concept for confining the methanol vapors and, after injection, the water or methanol mist is roughly separated from the scavenging air and then filtered using active carbon filters.

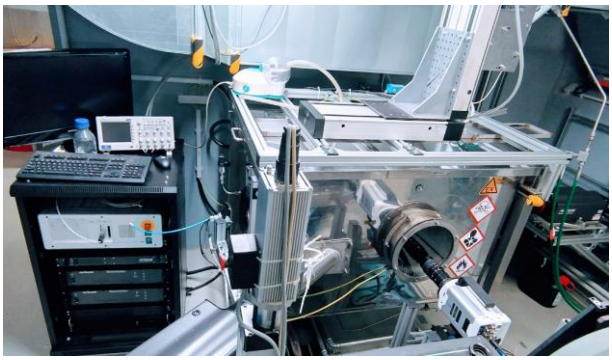

Figure 8: Particle Distribution and Spray test bench for analyzing methanol sprays.

The droplet size measurements were carried out using an Artium Phase Doppler Interferometer and were performed with an optics having a focal length of 2000 mm, in order to accurately capture also larger droplets, which, although limited in number, have large impact on the estimation of the Sauter Mean Diameter (SMD in the following), which was chosen as main metric of the spray droplet size.

The PDI measurements were performed at injection pressures of 10 bar and 25 bar, to match the pressure differential of 15 and 30 bar injection pressure and 5 bar counter pressure in the intake duct. The measurement locations were set in polar coordinates as the distance from the nozzle and the cone half angle. The nozzle distances chosen for this investigation ranged between 100 and 340 mm in the radial direction. The spray was scanned in 1° intervals from 52° to 58° half cone angle and all the measurement taken at a certain radial position were combined to obtain the particle size distribution at that location.

Finally, to gain a basic understanding of the spatial location and temporal evolution of the spray, high speed videos were captured of the entire spray cone and of the near nozzle region. For these measurements, a Photron Nova camera was used. The spray was illuminated from two sides by xenon light flashes.

3.2 Spray measurements results

Figure 9 depicts the spray evolution in the first instants after start of energization. It can be noticed how, in the immediate vicinity of the nozzle, the liquid sheet becomes unstable and breaks up. From these images, the cone half-angle could be determined to be 56,5 degrees. Figure 10 visualizes a typical particle distribution for all radial measurement locations across the spray at a fixed nozzle distance. The particle size distribution shows the expected log-normal shape, proving the accuracy of the measurement setup and procedure.

Figure 11 and Figure 12, instead, report the measured SMD for different injection pressures and nozzle distances for an injection of water and methanol respectively. It can be observed that at the furthest measurement location, the measured SMD for a methanol injection is between 44% and 52% of the corresponding injection pressure for a water injection. Moreover, in Figure 11 different trends of the SMD can be observed for different injection pressures: while for the 10 bar case, the SMD is almost constant for all the measurement distances, for an injection pressure of 25 bar a clear reduction of SMD occurs between nozzle distances of 100 mm and 340 mm. This can be explained by observing the 2D histograms of droplet velocity and droplet size reported in Figure 13.

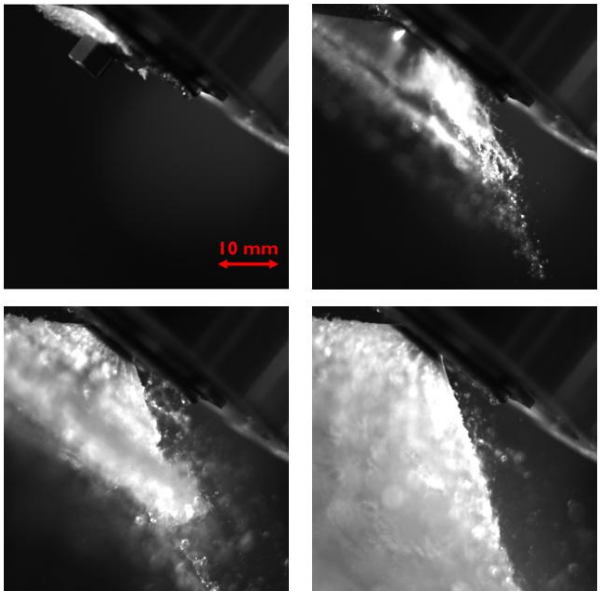

Figure 9: Spray evolution at 25 bar injection pressure for 1ms (*top left*), 2ms (*top right*), 4ms (*bottom left*) and 6ms (*bottom left*) after start of energization.

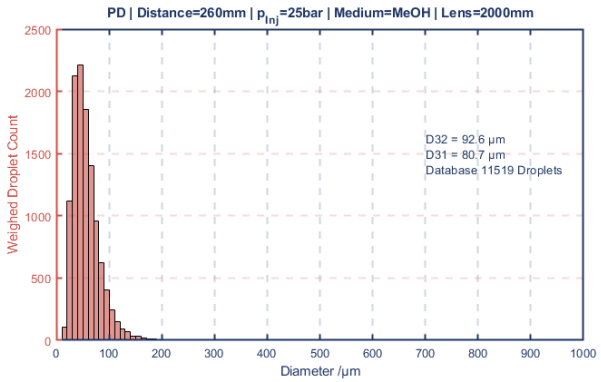

Figure 10: Particle size distribution for methanol injection, for an injection pressure of 25 bar and nozzle distance 260 mm.

When the injection pressure is set to 10 bar, very few droplets with a droplet Weber number greater than 12 are generated, where the droplet Weber number is defined as

$$We = \rho U^2 D/\sigma \quad (1)$$

where ρ is the air density, U is the initial relative velocity between the droplet and the surrounding air, D is the droplet diameter, and σ is the surface tension of the droplet. $We > 12$ is the threshold for triggering secondary breakup of a droplet via the bag-breakup mechanism [10], hence in this case no drastic inertially driven fragmentation of the droplets occurs, and the SMD remains almost constant along the evolution of the spray. With an injection pressure of 25 bar, instead, a large portion of the droplets present at a nozzle distance of 100mm have $We > 12$, hence these droplets will undergo secondary instability during the spray evolution, producing smaller droplets and consequently a reduction of the SMD.

The same type of evolution occurs also for an injection of methanol, but in this case the lower surface tension of methanol decreases the speed and diameter threshold for which a droplet becomes critical (see Figure 14), hence the evolution is observed already for an injection pressure of 10 bar. For the highest injection pressure of the methanol case, the reduction of SMD during the spray evolution, although present, is less evident: this can be explained by the already small dimensions of the droplets at the measurement location closest to the needle.

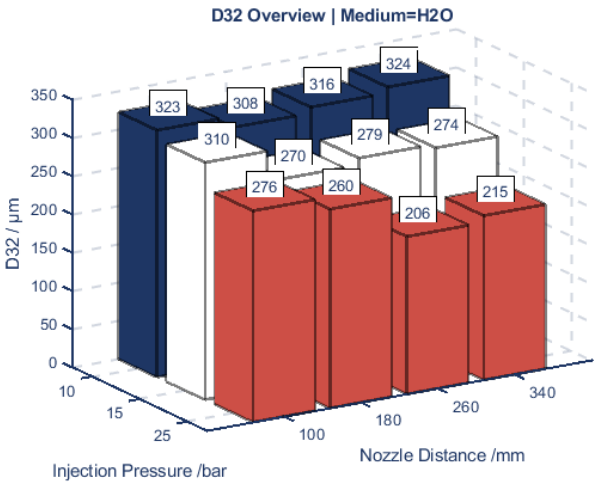

Figure 11: Sauter Mean Diameter measured at different locations and different injection pressure for a water injection.

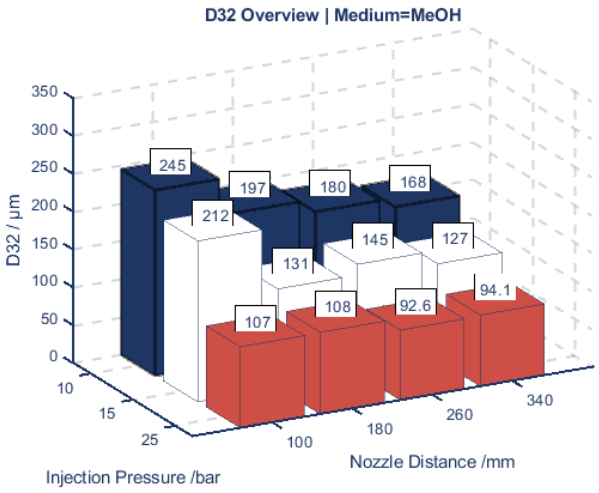

Figure 12: Sauter Mean Diameter measured at different locations and different injection pressure for a methanol injection.

3.3 CFD simulations setup and validation

In this study, the simulations were performed with the open-source OpenFOAM CFD code, where the solver was specifically adapted for the spray simulation under engine-relevant conditions [11]. The Reynolds-Averaged Navier Stokes (RANS) approach was used for describing the gas phase while turbulence was modeled using the standard $k-\varepsilon$ model with the so-called round jet correction: $C1$ was increased to 1.50 to predict the penetration of the fuel vapor jet [12], which is a common practice in simulating spray and turbulent gas jets. The PISO algorithm was used to couple pressure and velocity equations, ensuring accuracy in transient flow problems [13]. The evolution of liquid spray was computed using a Discrete Droplet Method (DDM), where the spray is assumed to be composed of a set of computational parcels, each one representing droplets with the same properties. Parcels evolve into the CFD domain in a Lagrangian fashion, exchanging mass, momentum, and energy with the continuous gas phase.

Specific sub-models are essential to mimic fuel atomization, breakup, heat transfer and evaporation. In the present work, the primary breakup was modeled by the Linearized Instability Sheet Atomization (LISA) model developed by Schmidt et al [14,15], which is typical for modeling the primary breakup of the liquid film emerging from outwardly opening injectors.

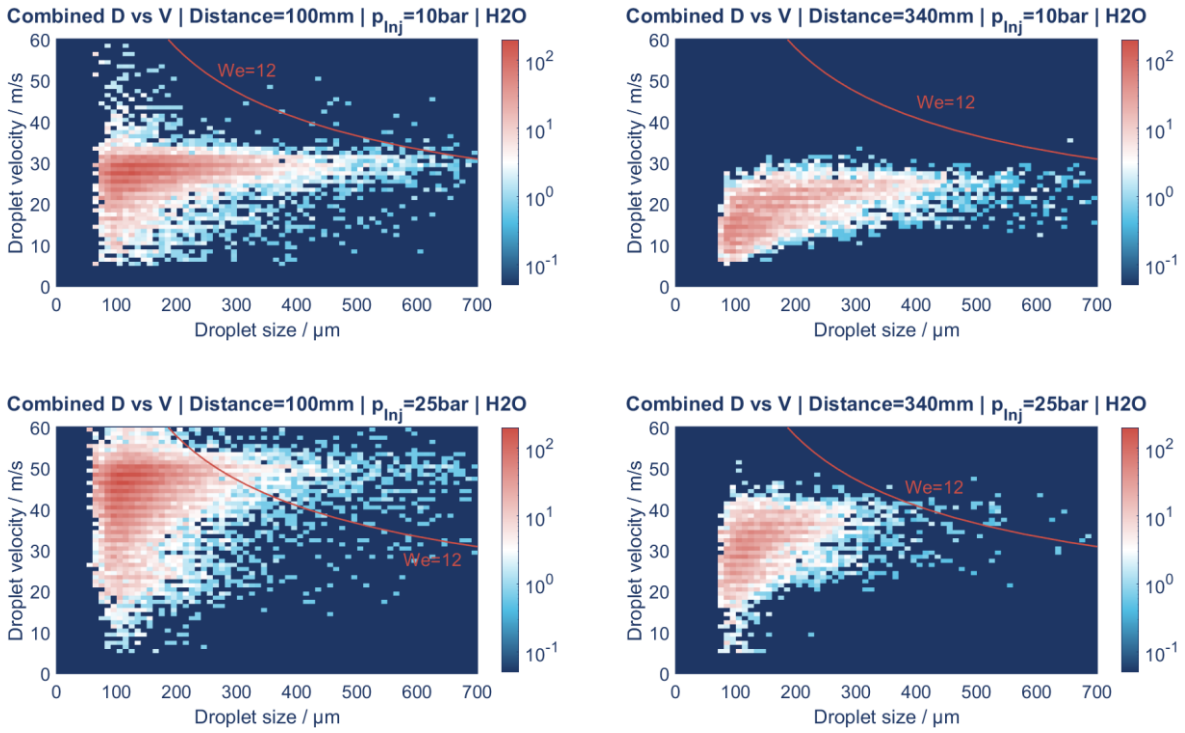

Figure 13: 2D histograms of droplet velocity and droplet size for a water injection with p_{inj}=10bar (*top*) and p_{inj}=25bar (*bottom*) at distances 100mm (*left*) and 340mm (*right*). Red solid line represents We=12.

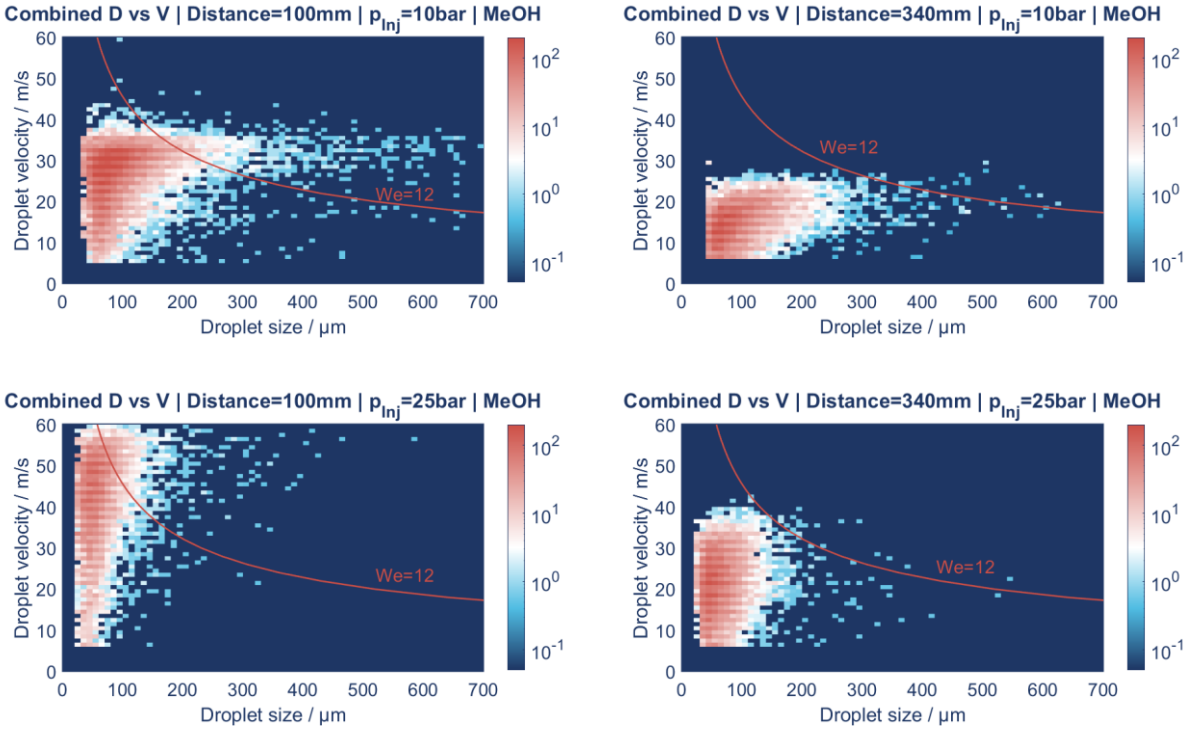

Figure 14: 2D hystograms of droplet velocity and droplet size for a methanol injection with p_{inj}=10bar (*top*) and p_{inj}=25bar (*bottom*) at distances 100mm (*left*) and 340mm (*right*). Red solid line represents We=12.

It was followed by activating the Reitz-Diwakar model [16,17], which reduces the second breakup to a continuous decrease in droplet radius. Droplet evaporation was computed from the droplet size and Spalding mass number while the Ranz-Marshall correlation was used to model heat transfer between the liquid and the surrounding gas phase. The simulations were performed in a 3D domain (600x600x380 mm) with periodic (cyclic) boundary conditions as illustrated in Figure 15, where the injection axis and the spray region are depicted. The grid was refined near the injector and its resolution progressively decreases when moving downstream of the injector to reduce the computational time, resulting in about 9.4 million cells with a minimum cell size of 1.25 mm. This resolution is adopted following a mesh sensitivity analysis conducted by the authors (but not presented here), which showed that the chosen resolution was a good compromise between computational efforts and prediction accuracy.

In order to validate the simulations against the experimental results discussed in §3.2, the same injection pressures of 25, 15, and 10 bar were considered, and the initial condition of the discharge chamber was quiescent air.

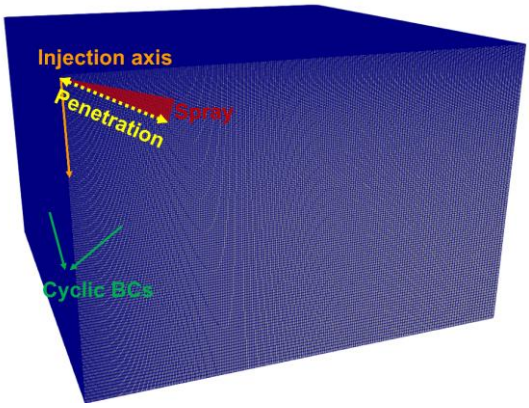

Figure 15: Computational domain and mesh.

The measured and computed liquid penetrations are compared in Figure 16, where the liquid penetration is defined as the maximum distance from the spray to the injector (a schematic illustration is shown in Figure 15). The results demonstrate that the simulation setup can accurately predict the liquid penetration at different injection pressures, which is essential for a correct description of the wall impingement process under real engine conditions.

The measured and computed droplet SMD at different injection pressures are compared in Figure 17, where the SMD is averaged across the entire injection process at different penetration distances: 180, 260, and 340 mm. It is possible to see that the simulation correctly captures the SMD trend across varying injection pressures, which reflects a change of relative velocity, giving us confidence in applying it to crossflow condition investigations.

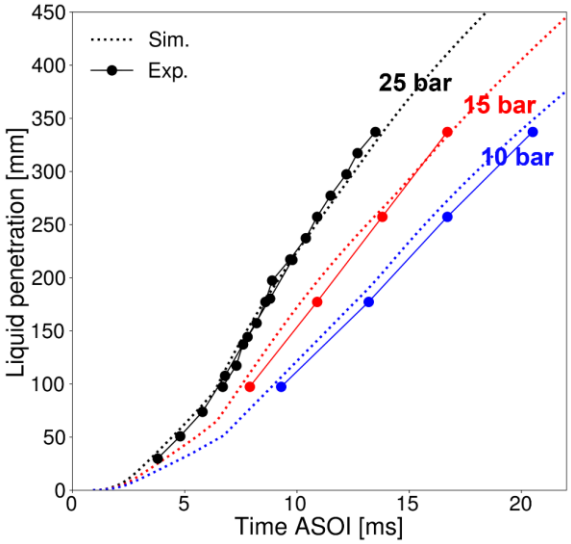

Figure 16: Measured and computed liquid penetration for different injection pressures.

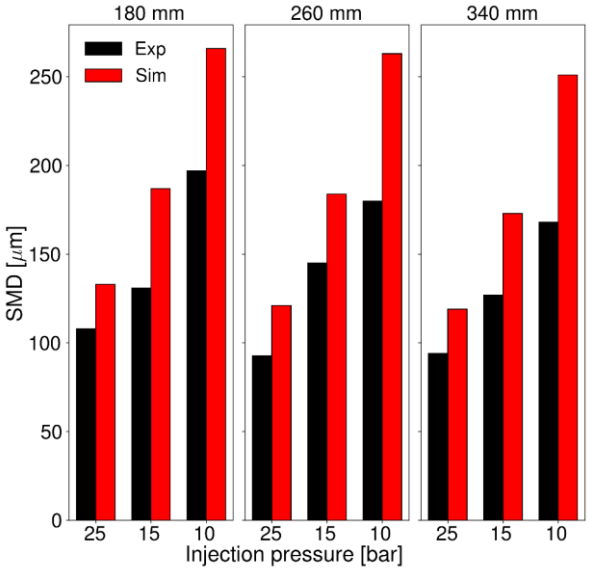

Figure 17: Measured and computed averaged SMD at different locations and injection pressures.

3.4 CFD simulations results with crossflow

Following the validation of the numerical setup, simulations were conducted under crossflow conditions, to simulate the injector spray evolution under more realistic conditions than the one which could be experimentally achievable. The injector was placed on the wall of an intake duct simplified as a pipe with a diameter of 140 mm and a length of 600 mm, the air speed was set at 85 m/s and the

air pressure was set at 5 bar. The injection point was positioned at the center of the pipe, as shown in Figure 18, which illustrates the cross-section of the computational mesh, having a minimum cell size of 0.7 mm and a total of 4.8 million cells to ensure the accurate flow and spray description. For clarity in the subsequent discussion, axis definitions are included: the y-axis denotes the flow direction, while the z-axis is oriented perpendicular to the pipe. The numerical study focuses on two key aspects: the effect of air and fuel temperatures, and the impacts of the injector mounting angle on methanol spray behaviors and wall impingement.

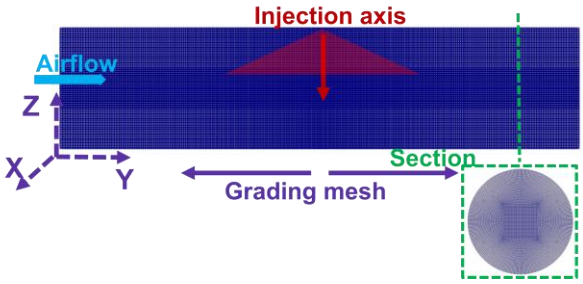

Figure 18: Computational mesh.

3.4.1 Air and fuel temperature variations

The study considered an air temperature range of 60°C to 80°C, where 60°C represents the typical air temperature after the cooler at 100% engine load. Fuel temperatures were varied between 45°C and 90°C. The overall SMD at the pipe exit for different air and fuel temperatures is shown in Figure 19. The results indicate that the impact of air and fuel temperature on the overall SMD is minimal within the considered range, with the SMD remaining around 30 µm. This demonstrates the injector's effectiveness in generating small droplets.

Figure 20 presents the ratio of vapor-phase methanol to the total methanol mass flow rate under different conditions. The results demonstrate that both air and fuel temperatures have a similar impact on evaporation, with higher temperatures leading to faster evaporation rates and higher vapor ratios. This behavior aligns with the evaporation model employed in this study, where the evaporation rate for a single droplet is expressed as:

$$\frac{dm_d}{dt} = -\pi d D_v \rho_v Sh \, ln\left(\frac{p - p_{v,\infty}}{p - p_{v,s}}\right) \quad (2)$$

Here the subscript v denotes the fuel vapor close to the droplet surface, with its properties evaluated at the film temperature, which follows the empirical 1/3 rule:

$$T_f = (2T_d + T)/3 \quad (3)$$

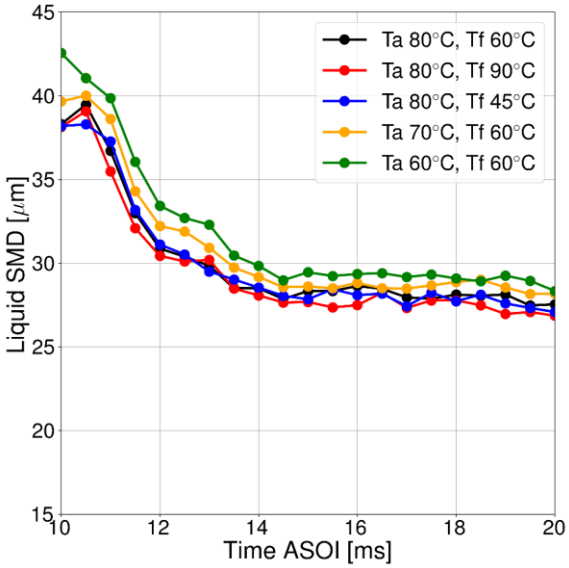

Figure 19: Overall SMD for different air and fuel temperatures at pipe exit.

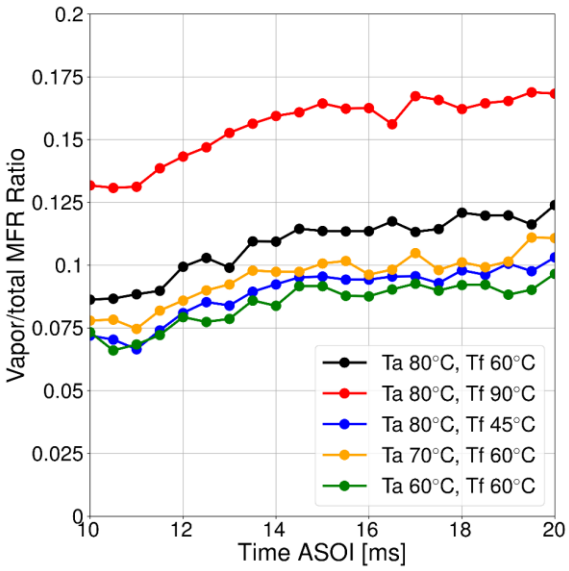

Figure 20: The ratio of vapor to total methanol mass flow rate for different air and fuel temperatures at pipe exit.

As a result, changes in air (T) and fuel (T_d) temperatures produce a similar trend in evaporation behavior. While fuel temperature shows a slightly greater influence on evaporation compared to air temperature, this difference is not visually noticeable due to the relatively small variations in the considered temperature range. It is worth noting that with a fuel temperature of 90°C and an air temperature of 80°C, approximately 16% of the methanol is in the vapor phase at the pipe exit. Further increasing the air temperature would be restricted by the engine air and power density requirements.

The average gas temperature at the pipe exit is illustrated in Figure 21, along with the temperature drop caused by the methanol injection. Such temperature drop can be attributed to two factors: sensible heat transfer due to the temperature difference between the liquid and the gas, and latent heat transfer due to the droplet evaporation. The overall temperature drops vary for different air and fuel temperatures: when the air temperature increases from 60°C to 80°C, the temperature drop ranges from 9.5°C to 15.2°C with about 1.2% increase in vapor ratio. When the fuel temperature increases from 45°C to 90°C, the temperature drop changes by approximately 3.3°C, despite around 7% increase in vapor ratio. This limited change is primarily due to the lower latent heat of vaporization at elevated fuel temperatures and the reduced sensible heat transfer or even negative when the fuel temperature is higher than the air. To achieve efficient and stable control of the engine air supply, the following conditions are desirable:

- The minimum gas temperature remains above the water saturation temperature to prevent condensation.
- The overall air temperature should not be excessively high to avoid abnormal operation and maintain power density.
- The system should achieve sufficient fuel evaporation to ensure proper mixing and combustion.

Considering these criteria and the findings from the investigation, a moderate air temperature combined with a high fuel temperature appears to be an optimal solution, providing effective fuel evaporation while minimizing excessive temperature drops in the intake system. Increasing fuel temperature, however, increases the risk of cavitation, and hence cavitation induced wear, at the nozzle exit. The effect of such fuel temperature on the injector lifetime needs still to be assessed in detail.

It is important to note that the surface film model was not included in the simulation. Therefore, the formation of liquid films on the intake duct walls could not be directly modeled. Instead, the spray mass (liquid methanol) in the cells adjacent to the walls was used to quantify the spray wall impingement area and the spray mass deposited on the walls. The results are presented in Figure 22, where the spray pattern is depicted, and the wall impingement area is highlighted with a red dashed line. The figure demonstrates that using the liquid mass in the cells effectively captures the wall impingement behavior. It is also possible to see that the changes in fuel and air temperature have minimal impact on the spray wall impingement area. This is because the impingement occurs approximately 100 mm from the injector, where droplet evaporation plays a limited role in reducing liquid penetration. Additionally, due to the large spray cone angle, wall impingement is less prominent on the lower section of the pipe but more concentrated on the side walls.

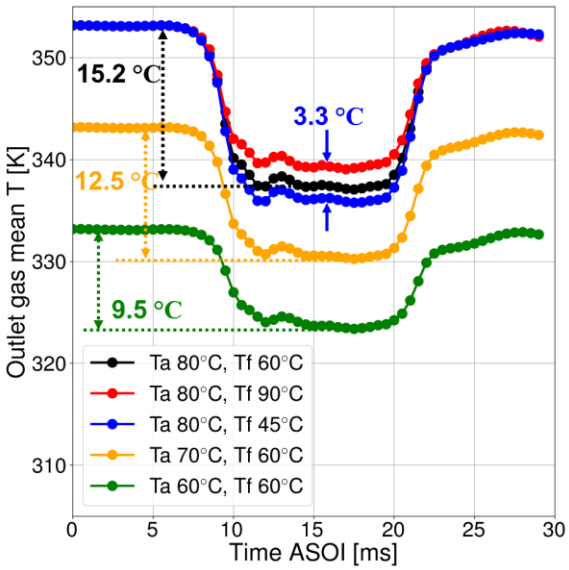

Figure 21: Average gas temperature for different air and fuel temperatures at pipe exit.

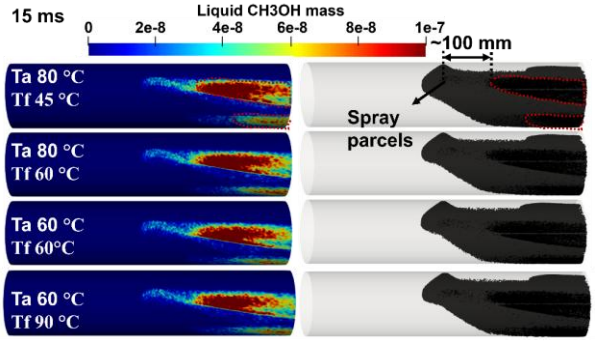

Figure 22: Liquid droplet mass impinging on the pipe wall for different air and fuel temperatures.

When comparing droplets exiting from the upstream and downstream sides of the injection axis, the initial droplet velocity is symmetric relative to the x-axis. Droplets on both sides have identical initial velocities in the z and y directions, but their velocities along the x-axis are of equal magnitude with opposite directions, with the ones from the upstream side being opposite to the flow direction (defined as negative). As a result, droplets from the upstream side take longer to travel downstream while requiring a similar amount of time to reach the walls, thereby increasing their likelihood of wall

impingement. This finding suggests that increasing the initial velocity component along the x-axis on the upstream side, for instance by adjusting the injector mounting angle, could help reduce wall impingement. This potential mitigation strategy will be further discussed in the next section.

3.4.2 Injector mounting direction variations

The effect of different mounting directions was studied under 80°C air temperature and 60°C fuel temperature conditions, where the simulations were performed for 5 angles: -25°, -12.5°, 0°, 12.5°, and 25°. Here, 0° represents the case where the injection axis is perpendicular to the intake duct. Negative angles indicate counterflow injection, while positive angles represent coflow injection. The 25° angle represents the maximum mounting position, as any further increase would cause the part of the spray to be directed toward the wall. A schematic of the various injection configurations is shown in Figure 23. The patterns shown in the schematic illustrate the initial droplet velocity at the nozzle exit for different mounting angles. The change in initial droplet velocity U_d when transitioning from counterflow to coflow can summarized as follows:

1. The overall droplet velocity magnitude $|U_d|$ remains unchanged, as it is governed by the injection mass flow rate and discharge coefficient.
2. The y component $U_{d,y}$ increases and transits from negative to positive, indicating a change in flow direction.
3. The magnitude of z component $|U_{d,z}|$ increases on the upstream side of the injection axis but decreases on the downstream side.
4. The x component $U_{d,x}$ remains unchanged.

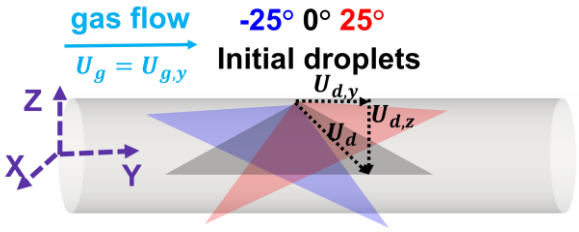

Figure 23: Schematic of different mounting angles.

The initial relative velocity magnitude between gas and liquid $|U_d - U_g|$ can be expressed and simplified as $\sqrt{{U_d}^2 + {U_g}^2 - 2U_{d,y}U_{g,y}}$. It is evident that as $U_{d,y}$ increases during the transition from counterflow to coflow, the relative velocity at the nozzle exit decreases for all the droplets across the entire injection disk. This reduction in relative velocity leads to less spray breakup, resulting in a larger SMD, as shown in Figure 24, which presents the overall droplet SMD in the pipe for various mounting angles.

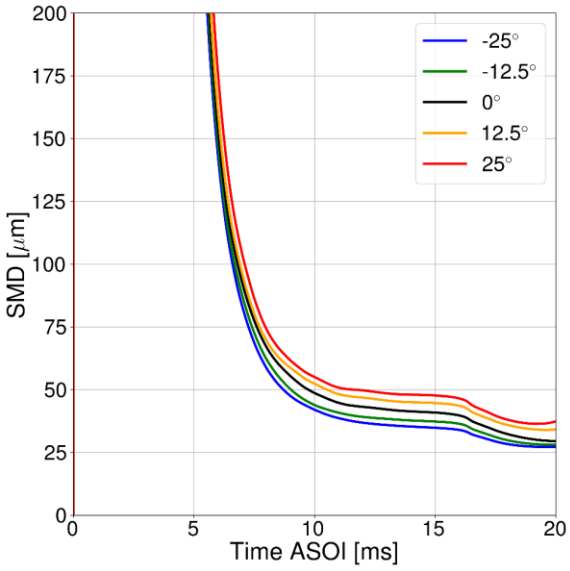

Figure 24: Overall SMD in the pipe for different mounting angles.

This consequently lowers the evaporation rate, as shown in Figure 25, which presents the vapor-to-total methanol mass flow ratio at the pipe exit. Increasing the injection angle from 0° to 25° leads to a 1.5% reduction in vapor ratio. Figure 26 illustrates the overall SMD at the pipe exit. Unlike the overall SMD inside the pipe, the SMD at the pipe exit is more influenced by whether the injection is coflow or counterflow rather than by the variation in absolute mounting angles. This behavior can be attributed to the complex interaction between spray breakup, evaporation dynamics, and final droplet velocity. Despite these differences, the overall SMD at the pipe exit remains low, ranging from 25.7 to 32.5 µm when transiting from counterflow to coflow (at ~15 ms), due to the effective atomization provided by the injector and the high air velocity in the pipe.

For a more detailed analysis, the clip of the spray patterns along the xz plane at 15 ms for various mounting angles are illustrated in Figure 27, with the color scales representing the droplet diameter and x velocity component. The figure allows for an approximate distinction between the main spray patterns originating from the upstream and downstream sides of the injection axis by examining the droplet size distribution, which is also depicted. Two main observations can be made as the injection shifts from counterflow to coflow:

- Droplets on the upstream side of the injection axis exhibit an increase in $|U_{d,z}|$, resulting in greater penetration along the z-axis. On the downstream side, droplets have a lower $|U_{d,z}|$ and penetrate toward the upper section of the pipe, where the distance to the wall is shorter, increasing the risk of wall impingement.
- There is an increase in $U_{d,y}$ for droplets from both upstream and downstream sides, speeding up their movement toward the exit of the pipe, which could reduce the spray impingement area.

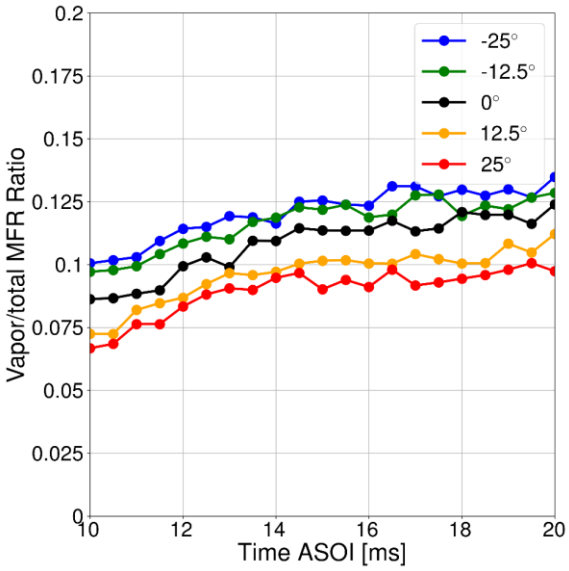

Figure 25: The ratio of vapor to total methanol mass flow rate at pipe exit for different mounting angles.

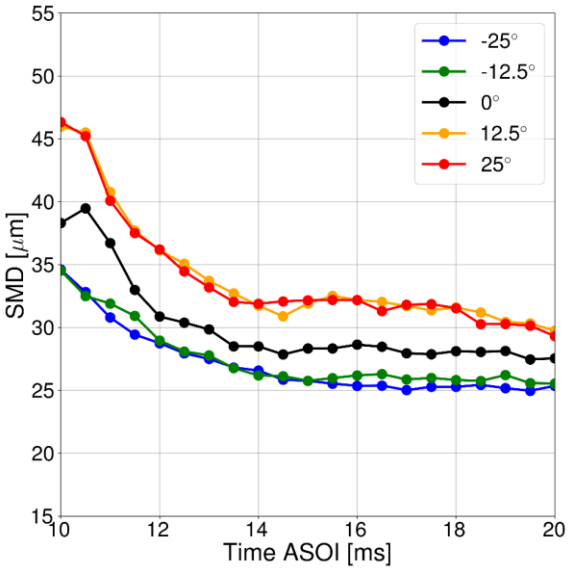

Figure 26: Overall SMD at pipe exit for different mounting angles.

The second factor plays a more dominant role within the tested range of mounting angles, as can be seen in Figure 28, which shows the liquid droplet mass impinging on the pipe wall at different time instants for different mounting angles from both the side view (along the x-axis) and the bottom view (along the z-axis, from bottom to top), the spray impingement area can be significantly reduced when transitioning from counterflow to coflow mounting direction.

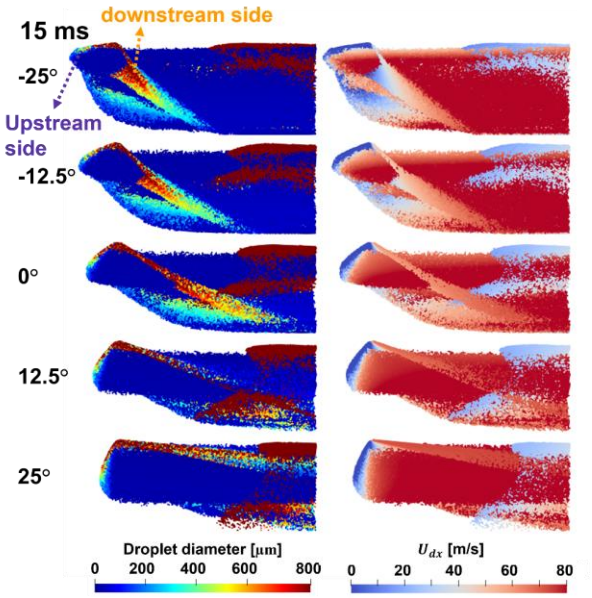

Figure 27: Droplet size and velocity at 15 ms for different mounting angles.

4 CONCLUSIONS

In this paper, the design of the OMT methanol port fuel injector for engines with power up to 1200kW/cylinder was presented and the main design choices were illustrated. It was shown that, with an outward-opening poppet valve architecture, large volume flow rates can be achieved, while minimizing the characteristic length scale of the injected fluid film, hence maximizing the quality of atomization. Measured injector performance closely matched simulated behavior, and good injection repeatability was achieved.

To characterize the spray generated by the injector, a new test bench was designed and built at FVTR, allowing OMT to safely perform PDI and other measurements with low viscosity fuels like methanol. Measurement results with methanol showed that the OMT injector is capable of generating a fine spray, with an SMD in quiescent air of approximately 100μm, at a distance of 100mm from the nozzle.

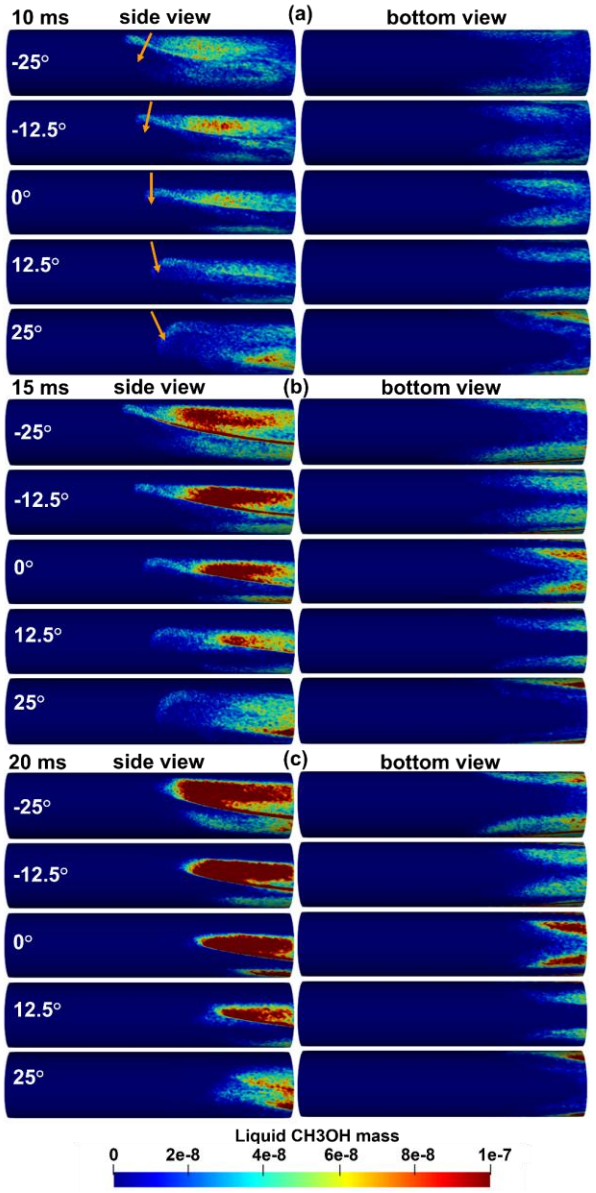

Figure 28: Liquid droplet mass impinging on the pipe wall at different time instants for different mounting angles.

To better understand the behavior of the injector under real-life engine conditions, a CFD study of the spray behavior was performed by the Accelleron Advanced Technology team. The model was capable of correctly describing the experimental trends, and it showed that an SMD of about 30µm is achieved for an injection in an engine intake duct. Variation of the fuel and intake air temperatures were considered, and it was concluded that a fuel temperature increase of 30°C at fixed intake air temperature can lead to a nearly 50% increase in vapor mass flow rate.

The effect of the injector mounting angle was also studied, and it was found that installing the injector slightly tilted toward the downstream direction can help minimize the wall impingement of the spray, with minimal negative effect on the SMD. The CFD model developed will also help to evaluate the spray behavior for different operating conditions, needle lifts, and spray cone angles.

Combined experimental and CFD results show that the OMT PFI is a practical and easily installed technology which will enable the marine industry to retrofit a substantial population of existing ship engines to run on methanol. Depending on the availability of green methanol, this breakthrough could significantly advance decarbonization in the next several years.

5 ACKNOWLEDGMENTS

The authors would like to acknowledge the work of the team of OMT for their support and dedication to achieve the results reported in this paper, and Fabian Pinkert of FVTR GmbH for performing the spray tests and for the interesting and fruitful discussions during the data analysis.

6 REFERENCES AND BIBLIOGRAPHY

[1] International Maritime Organization, 2023. 2023 IMO Strategy on Reduction of GHG Emissions from Ships, Resolution MEPC.377(80), London, United Kingdom.

[2] Coppo, M., et al., 2023. Powering a greener future: the OMT injector enables high-pressure injection of ammonia and methanol, *CIMAC Congress*, Busan, South Korea, paper 139.

[3] DNV, 2023. Maritime Forecast to 2050 – Energy Transition Outlook 2023, Høvik, Norway.

[4] Bhuvaneswaran M, et al., 2024. Development of dual fuel methanol engine using CFD techniques for PFI and HPDI injection strategies, *8th Rostock Large Engine Symposium*, Rostock, Germany, 1:36-55.

[5] Yin, X., et al., 2023. In-depth comparison of methanol port and direct injection strategies in a methanol/diesel dual fuel engine*, Fluid Processing Technology*, 241: 107607.

[6] Altun, Ş. et al., 2023. Comparison of direct and port injection of methanol in a RCCI engine using diesel and biodiesel as high reactivity fuels, *Process Safety and Environmental Protection*, 174: 681-693.

[7] International Chamber of Shipping, 2024. Global Fleet Statistics.

[8] Kooij S. et al., 2018. What determines the drop size in sprays?, *Physical review X*, 8:031019.

[9] Hiroyasu H. and Arai M., 1990. Structures of Fuel Sprays in Diesel Engines, *SAE Transactions*, 99: 1050–1061.

[10] Pilch, M. and Erdman, C.A., Use of breakup time data and velocity history data to predict the maximum size of stable fragments for acceleration-induced breakup of a liquid drop, *International Journal of Multiphase Flow*, 13(6): 741-757.

[11] Zhou, Q., Lucchini T. et al., 2022. CFD Modeling of Impinging Sprays Under Large Two-Stroke Marine Engine-Like Conditions, *SAE Technical Paper* 2022-01-0493.

[12] Pope, S.B., 1978. An explanation of the turbulent round-jet/plane-jet anomaly, *AIAA Journal*, 16:279-281.

[13] Ferziger, J.H. and Perić, M., 2002. *Computational Methods for Fluid Dynamics*, Springer, Berlin, Heidelberg, Germany.

[14] Schmidt D. P. et al., 1999. Pressure-Swirl Atomization in the Near Field, *SAE Technical Paper* 1999-01–0496.

[15] Senecal, P.K. et al., 1999. Modeling high-speed viscous liquid sheet atomization, *International Journal of Multiphase Flow*, 25(6): 1073–1097.

[16] Reitz, R.D., 1987. Modeling atomization processes in high-pressure vaporizing sprays, *Atomisation Spray Technology*, 3:309–337.

[17] Reitz, R.D. and Diwakar, R., 1986. Effect of Drop Breakup on Fuel Sprays, *SAE Technical Paper* 860469.